



The formation of magnetite in the early Archean oceans



Yi-Liang Li^{a,*}, Kurt O. Konhauser^b, Mingguo Zhai^c

^a Department of Earth Sciences, the University of Hong Kong, Hong Kong, China

^b Department of Earth and Atmospheric Sciences, University of Alberta, Canada

^c Institute of Geology and Geophysics, Chinese Academy of Science, China

ARTICLE INFO

Article history:

Received 30 September 2016

Received in revised form 5 March 2017

Accepted 7 March 2017

Available online xxxx

Editor: D. Vance

Keywords:

Archean

banded iron formation

photosynthetic Fe(II)-oxidation

magnetite

green rust

deep-sea hydrothermal fluid

ABSTRACT

Banded iron formations (BIFs) are iron- and silica-rich chemical sedimentary rocks that were deposited throughout much of the Precambrian. The biological oxidation of dissolved Fe(II) led to the precipitation of a ferric oxyhydroxide phase, such as ferrihydrite, in the marine photic zone. Upon burial, ferrihydrite was either transformed into hematite through dehydration or it was reduced to magnetite via biological or abiogenic Fe(III) reduction coupled to the oxidation of buried microbial biomass. However, it has always been intriguing as to why the oldest BIFs are characteristically magnetite-rich, while BIFs formed after the Neoproterozoic are dominated by hematite. Here, we propose that some magnetite in early Archean BIF could have precipitated directly from seawater through the reaction of settling ferrihydrite and hot, Fe(II)-rich hydrothermal fluids that existed in the deeper waters. We conducted experiments that showed the reaction of Fe(II) with biogenic ferric iron mats under strict anoxic conditions lead to the formation of a metastable green rust phase that within hours transformed into magnetite. Our model further posits that with the progressive cooling and oxidation of the Earth's oceans, the above reaction shuts off, and magnetite was subsequently restricted to reactions associated with diagenesis and metamorphism.

© 2017 Elsevier B.V. All rights reserved.

1. Introduction

Banded iron formations (BIFs) are one of the most important sedimentary archives for understanding Precambrian ocean chemistry and the evolution of the marine biosphere (e.g., Bekker et al., 2010, 2014). Two types of BIF have been recognized with respect to their depositional setting. Algoma-type BIF are stratigraphically linked to submarine-emplaced volcanic rocks in greenstone belts and, in some cases, with volcanogenic massive sulfide deposits (Ohmoto, 2003). They range in age from Eoarchean to early Paleoproterozoic, which possibly reflects the absence of large, stable cratons at that time (Isley and Abbott, 1999). Superior-type BIF, which becoming common in the late Archean to Paleoproterozoic, were deposited in the near-shore continental-shelf environments, and are typically interbedded with carbonates, quartz arenite, and black shale, but with only minor amounts of volcanic rocks (Klein, 2005). Unlike most Algoma-type BIF, which rarely extend for more than 10 km along strike and are usually not more than 50 m thick, the Superior-type BIF can be extremely laterally extensive, with original extents estimated in some cases to be over 100,000 km² (Morris, 1993; Isley and Abbott, 1999). Superior-type

BIF first appear in the late Archean, when construction of large continents first began. From ca. 2.6 to ca. 2.4 Ga, global mafic magmatism culminated in the deposition of giant Superior-type BIF in South Africa, Australia, Brazil, Russia, and Ukraine (Isley and Abbott, 1999).

BIF are dominated by silica (~40–50%) and iron oxides (~20–40%). The mineralogy of the least metamorphosed BIF consists of chert (SiO₂), magnetite (Fe₃O₄), hematite (Fe₂O₃), siderite (FeCO₃) and various iron-silicate minerals, such as greenalite ((Fe)₃Si₂O₅(OH)₄): the presence of both ferric and ferrous minerals gives BIF an average oxidation state of Fe^{2.4+} (Klein, 2005). It is generally agreed that none of the minerals in BIF are primary, but that instead, the minerals reflect both diagenetic and metamorphic overprinting. For instance, hematite is believed to be a dehydrated product of a ferric hydroxide precursor, such as ferrihydrite, precipitated in the photic zone via enzymatic oxidation (Kappler et al., 2005) or oxidation by O₂ derived from oxygenic cyanobacteria (Planavsky et al., 2014). This view was recently supported by Sun et al. (2015) who conducted high resolution transmission electron microscopy (TEM) and selected area electron diffraction (SAED) of fine mineral structures in BIF from the 2.73 Ga Abitibi greenstone belt in northwestern Canada and the 2.46 Ga Kuruman Iron Formation in South Africa to ascertain the timing and paragenesis of hematite. Sun et al. (2015) interpreted that the 3–5 nm ultrafine hematite crystals in the hematite bands and those submicrometer

* Corresponding author.

E-mail address: yiliang@hku.hk (Y.-L. Li).

(sub)ehedral hematite crystals randomly distributed in the chert matrix of transitional zones between iron oxide- and chert-rich bands were directly dehydrated from a precursor ferric hydroxide phase.

In terms of magnetite, a number of petrographic studies have described the mineral as being of sedimentary origin. For instance, Krapež et al. (2003) reported several forms of diagenetic magnetite, including (1) disseminated grains within but obscuring sedimentary laminae, (2) laminated beds that clearly truncated sedimentary layering, (3) layer-discordant veins, and (4) cleavage fills. Ewers and Morris (1981) even suggested that most magnetite in the BIF of the 2.48 Ga Dales Gorge Formation of Western Australia was secondary by showing overgrowth of a fine-grained ferric hydroxide precursor. Recently, Li et al. (2013) proposed a model to account for magnetite formation in BIFs that included a three-stage sequence, beginning with the biomineralization of magnetite by dissimilatory Fe(III) reduction (DIR) of an initial ferric iron-rich sediment coupled to the oxidation of dead phytoplankton biomass, followed by magnetite crystal aging, and ultimately pressure-temperature induced abiotic growth of the biogenic magnetite during metamorphism.

Five lines of evidence are in agreement with the notion that magnetite formation during diagenesis was initially driven by DIR. First, extant hyperthermophilic *Bacteria* and *Archaea* branch deeply in the universal phylogenetic tree (i.e., they represent an ancient metabolism) and can reduce Fe(III). Second, highly negative $\delta^{56}\text{Fe}$ values in magnetite-rich BIF samples as old as 2.9 Ga have been observed and are comparable to the negative fractionations measured in experimental culture with DIR bacteria (e.g., Johnson et al., 2008). Third, Li et al. (2011) conducted detailed crystallochemical analysis of magnetite from the Dales Gorge Member BIF and reported magnetite with a lattice constant and $\text{Fe}^{2+}/\text{Fe}^{3+}$ stoichiometry very similar to those produced by DIR bacteria including *Geobacter*, *Shewanella* and *Thermoanaerobacter*. Fourth, biogenic magnetite crystals have very pure chemical compositions, which is regarded as one of the major criteria for assigning a biogenic origin to magnetite (Li et al., 2011) – magnetite in BIF can also have a pure end-member composition (Gole, 1981). Fifth, recent experimental low-grade alteration of biogenic magnetite demonstrated how the fine-grained magnetite produced via DIR (a few hundred nm or smaller in size) can grow in size to nearly 1 micron upon reaction of ferrihydrite and microbial biomass under simulated low-grade metamorphic conditions (Li et al., 2013).

Despite the wide acceptance of a secondary origin for magnetite in BIF, it has always been puzzling why BIFs from the early Archean are predominantly composed of magnetite. For instance, the ~ 3.7 Ga BIFs from the Isua Supracrustal Belt (ISB) in Western Greenland (Frei and Polat, 2007; Czaja et al., 2013), 3.05–2.95 Ga Mount Gibson BIF in Western Australia (Lascelles, 2006), and 2.98 Ga West Rand Group of the Witwatersrand Supergroup, South Africa (Smith et al., 2013) contain mostly magnetite as the iron oxide phase. Gross (1986) reported that the early BIFs (prior to 2.6 Ga) have higher $\text{Fe}^{2+}/\text{Fe}^{3+}$ ratios in the oxide facies than those in the late stage, indicating a relatively high amount of magnetite in the early deposited BIFs. It is observed that the Archean BIFs are characterized by not only high abundance of magnetite, but also their high grade metamorphic grades (Klein, 2005). For example, the BIF of ISB is of amphibole metamorphic grade and with almost 100% magnetite as its oxide phase, but Fe-isotopic compositions of both stratigraphic bands and magnetite crystals within bands show features not influenced by metamorphic fluids (Frei and Polat, 2007; Czaja et al., 2013). By contrast, BIFs deposited after 2.6 Ga show a dramatic increase in hematite content. For instance, the 2.48 Ga Dales Gorge Formation (Li et al., 2011) and the 1.9–1.8 Ga Frere Formation in Western Australia (Klein, 2005) are mostly composed of hematite, as are the

many Neoproterozoic BIFs (Klein, 2005). On a related note, Gole (1981) showed that under the same grade of metamorphic alteration, $\text{Fe}^{3+}/\text{Fe}^{2+}$ in the magnetite-rich BIF is not higher than that of coexisting shale with high content of organic matter, implying later diagenetic or metamorphic processes might not be able to produce substantial amount of magnetite in BIFs. In terms of organic carbon content in BIF, it is extremely low and there is also no significant variation through time (Klein, 2005), suggesting that there was unlikely to have been more biomass production in the early Archean oceans than thereafter. In other words, the excess magnetite might not be a reflection of more organic carbon burial or enhanced DIR. Moreover, because negative $\delta^{56}\text{Fe}$ values are not found in the sedimentary record prior to around 2.9 Ga, Johnson et al. (2008) suggested that DIR did not have a large impact on the marine sedimentary record before that time.

Based on oxygen isotopic thermometry and silicon isotopic compositions in early Archean cherts, it has been estimated that seawater temperature could have been as high as 55–85 °C (Knauth, 2005). Therefore, it is possible that the higher magnetite content in Archean Algoma-type BIF might be due to the reaction of hot, Fe(II)-rich seawater with primary ferric hydroxides; the latter formed via photosynthetic Fe(II) oxidation – photoferrotochemistry – because to date this is the most accepted model in the absence of free oxygen (see Kappler et al., 2005; Konhauser et al., 2007; Pecoits et al., 2015). In other words, the key ingredients for the early formation of magnetite in the hot seawater rich with Fe(II) and ferric hydroxide precipitation were available in that window of time, but as the mean ocean temperature cooled and as the ocean water column became gradually oxygenated on the shelf, hydrothermal fluids cooled upon mixing, and ultimately the mechanism for magnetite formation ceased to exist. Certainly the REE patterns in Algoma-type BIFs, specifically the shale normalized europium (Eu) anomalies, have been central in showing that Archean BIFs record a strong influence of high-temperature hydrothermal fluids on the seawater dissolved REE (e.g., Jacobsen and Pimentel-Klose, 1988; Derry and Jacobsen, 1990; Isley and Abbott, 1999; Smith et al., 2013). In contrast, the REE patterns of BIFs precipitated in the Paleoproterozoic demonstrate waning hydrothermal input at that time (Derry and Jacobsen, 1990).

In this study we experimentally test the hypothesis that in the early Archean ocean, the episodic reaction of hot Fe(II)-rich hydrothermal fluids with biogenic ferric hydroxide led to the precipitation of magnetite. We reacted microbial induced ferric oxyhydroxides precipitates with dissolved Fe(II) under strictly anaerobic conditions and found the formation of magnetite, with green rust (GR) as the intermediate phase at temperatures in excess of 50 °C.

2. Sample and methods

2.1. Sample preparation

In this study we used ferrihydrite mats produced by *Gallionella* and *Leptothrix* from the Low Pond of Aberdeen Country Park, Hong Kong. Although these mats do not contain photoferrotochemical species as predicted for the Eoarchean oceans, ferrihydrite has been proved to be the only ferric oxyhydroxide in the Fe(II)-oxidizing mat (Lv et al., 2016). The low organic matter in those ferric iron biomats was suggested to be comparable to the biological precipitation of ferric oxyhydroxide precursors from the ferruginous ocean (Kappler et al., 2005; Swanner et al., 2015). By using this ferrihydrite mat, we could also test the possible role biomass might have played in the conversion of ferrihydrite to more stable iron oxides at higher temperatures in the Archean ferruginous waters.

The ferrihydrite mats of *Gallionella*–*Leptothrix* were returned to the laboratory and suspended in 0.05 M HEPES (2-[4-(2-hydr-

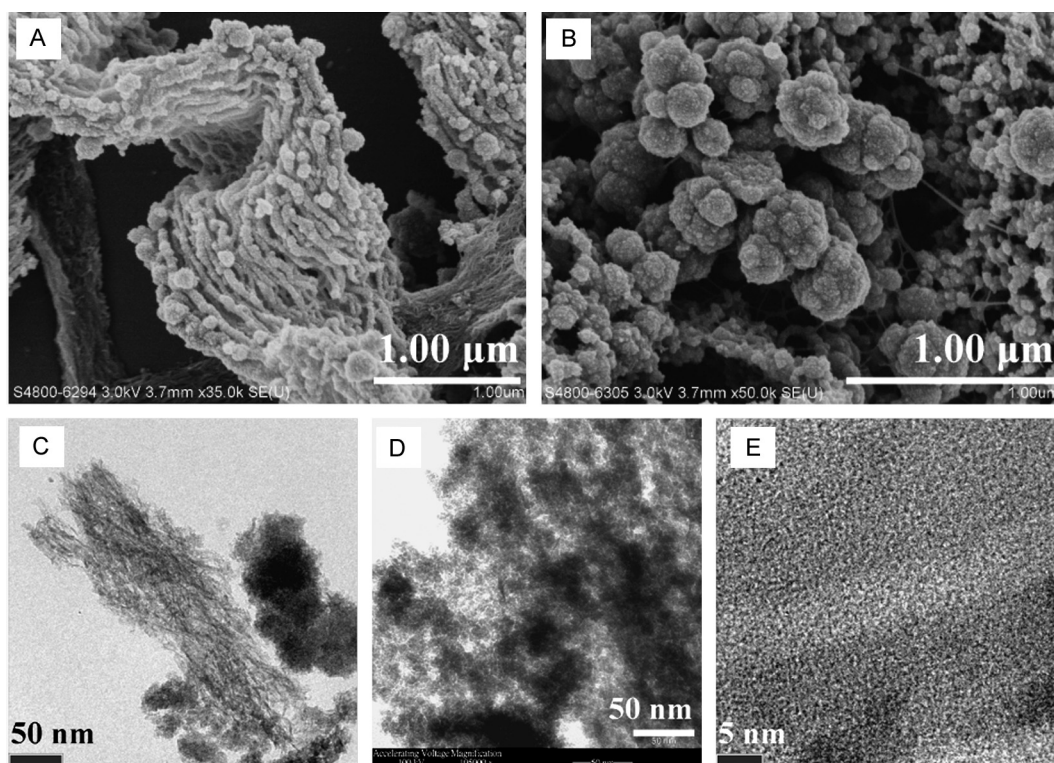


Fig. 1. SEM and TEM characterizations of original bacterial Fe(II)-oxidizing mats. The SEM observation of *Gallionella* stalk covered by ferric iron rusticles; B. SEM observation of ferric iron spherules; C–D. High resolution TEM observation of fibrils encrusted by amorphous ferrihydrite; E. High resolution TEM observation of ferrihydrite showing its amorphous nature.

oxyethyl)-1-piperazine]ethanesulfonic acid) buffered media with a solid/liquid ratio approximately 1 mg/ml. Samples were then adjusted to pH values of 7.5, 8.0 and 9.0, values that would have likely bracketed the predicted pH values of deep seawater in the Archean (e.g., [Jacobsen and Pimentel-Klose, 1988](#)). A 10 ml slurry was dispensed in each 26-ml pressure tube and bubbled with 100% N₂ for 20 min at room temperature to remove O₂ ([Butler et al., 1994](#)). The tubes were then sealed with butyl rubber stoppers and aluminum crimp-caps.

For comparison, strict anaerobic slurries of synthesized pure ferrihydrite and ultrafine hematite particles extracted from the 2.48 Ga Dales Gorge Member BIF were prepared by the same procedure. To extract hematite fine particles from the BIF, ~1 g iron oxide BIF was ground into fine powder and then mixed with 40 ml 100% ethanol in a 50 ml centrifuge tube. The extremely fine particles of hematite made a suspension while all the other particles (e.g., magnetite, chert and silicates) settled to the bottom of the tube. A magnet was applied to the tube to fix magnetite and a pipette was used to transfer the hematite suspension to another tube. The obtained hematite was a pure phase of ultrafine nanocrystals of 3–5 nm, as examined by TEM in a previous study ([Sun et al., 2015](#)).

2.2. Reaction between ferric iron oxide slurries and Fe(II) under strictly anaerobic conditions

After the injection of 1 ml 0.1 M (NH₄)₂Fe(SO₄)₂ stock solution, the slurries were gently shaken, stationed for 5 min at room temperature, and then incubated at temperatures of 40 °C, 50 °C and 60 °C. There was no loss of biomass through the preparation procedure. The media incubated at 60 °C turned to black after 10 h; similar phenomena were observed in media incubated at 50 °C after 5 days. However, the media incubated at 40 °C did not show substantial difference from the media containing synthesized ferrihydrite without the addition of Fe(II) placed at room temperature,

even after 40 days. After longer incubations (>2 months), all the slurry materials transformed into black precipitates. Tubes with chemically synthesized ferrihydrite displayed similar color changes to the natural ferrihydrite mats, but with faster reaction rates. The anaerobic slurry of hematite extracted from BIF was initially reddish brown but turned to light blue–green with the addition of Fe(II) solution. The color did not change at the end of two-month incubation.

2.3. SEM and TEM observations

A Hitachi S-4800 FEG scanning electron microscope (SEM) equipped with electron dispersive X-ray spectroscopy (EDS) was employed to characterize morphology and chemical composition of the minerals. A FEI Tecnai G2 20 S-TWIN TEM equipped with SAED and EDS was used to characterize the mineral structures and chemical composition of the ultrafine particles. Subsamples for electron microscopic studies were extracted at the electron microscopic laboratory immediately prior to loading in order to minimize any changes resulting from excessive exposure to the atmosphere. To do so, the sampling tubes were shaken and subsamples were taken out by syringe, treated by pure ethanol so that they could dry quickly, and loaded on either a silica slide for SEM observation or a copper grid for TEM observation.

2.4. Mössbauer spectroscopy and X-ray diffraction (XRD)

The black precipitates were dried by ethanol and placed in a 1-cm² acrylic holder to make iron concentrations equivalent to ~5 mg/cm² for Mössbauer spectroscopic measurements at room temperature. A 25 mCi ⁵⁷Co/Pb radioactive source was used, and a 25-μm α-Fe was measured before and after to calibrate the hyperfine parameters. The Mössbauer spectra were collected for incubated samples at 20 h, 30 h and 44 h, and fitted by using

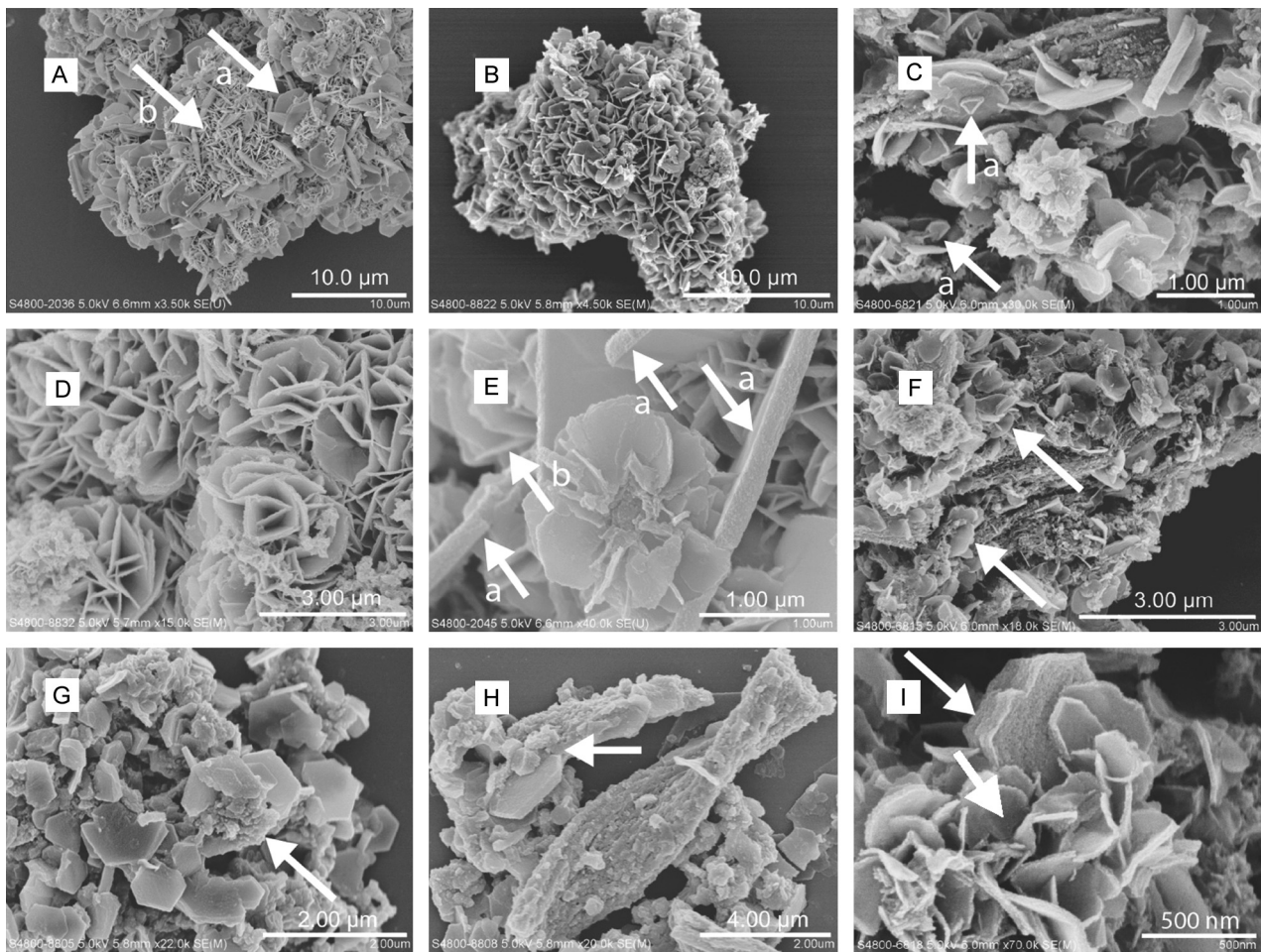


Fig. 2. SEM observations of the formation of green rust reactions between Fe(II) and ferrihydrite mats slurry under strict anaerobic condition. A. General view of GR aggregates made of flakes (arrowed) of different sizes; B. Well-defined green rust aggregates; C. Triangle crystal plane and foil-like structures observed among the green rust flakes; D. Rosette-like green rust aggregates; E. Rosette-like grain aggregates; F. Green rusts (arrowed) developing on the fibrous stalks; G. Well-defined GR developing on aggregates (arrowed) covered by colloidal material; H. Well-defined GR crystals growing on biogenic stalks (arrowed); I. The layer structure of GR crystals (arrowed).

WinNormos software based on least square fitting of Lorentzian line-shapes.

For powder X-ray diffraction (XRD) analysis, about 15 to 20 mg of the mineral end-products from the incubations were suspended with ethanol and placed on the plate holder. Samples were scanned from 10° to 80° for 2θ with a step of $0.02^\circ \text{ s}^{-1}$ by a Bruker D8 Advance diffractometer with Cu $K\alpha$ radiation (40 kV and 40 mA). The data were analyzed using software Jade 6.5.

3. Results

3.1. SEM and TEM observation of the intermediate phases

The electron microscopic mineralogical characterization of ferrihydrite-rich mats collected for the study have previously been described in Lv et al. (2016). As observed by SEM, spherulitic rusticles of a few tens to hundreds of nm could be observed on the surface of the stalks (Fig. 1A) or between the stalks (Fig. 1B) that were produced during bacterial Fe(II)-oxidation. High resolution TEM observations further showed that ferrihydrite was either on the surface of stalks (Fig. 1C) or made spherules (Fig. 1D) without biomass. TEM observations could not detect any crystal ordering (Fig. 1E), implying ferrihydrite in the biomats retained an amorphous nature until the experimental study.

In experimental samples with natural ferrihydrite mats plus dissolved Fe(II), SEM observations showed that the hexagonal platelets agglomerated into aggregates (Figs. 2A–D). Two groups of

hexagonal platelets with different sizes were observed: (1) 1–2 μm in diameter (Fig. 2A, arrow a) and >20 nm in thickness (Fig. 2E, arrow a), and (2) 400–600 nm in diameter (Fig. 2A, arrow b) and ~ 3 nm in thickness (Fig. 2E, arrow b). A small number of crystals with triangular planes (Fig. 2C, arrow a, ~ 10 nm in size) were observed. EDS measurements showed the triangular-planed crystals contained high Si and Fe (Si/Fe ~ 0.35) with composition and structure close to the mineral cronstedtite ($\text{Fe}_2^+ \text{Fe}_3^+ \text{SiO}_5(\text{OH})_4$), similar to previous reports (e.g., Pignatelli et al., 2013). A SAED pattern of a monocrystal was obtained but not shown here because it only yielded the diffraction of one crystal plane, which was not sufficient to confirm the crystal structure.

Rosette structures made of hexagonal GR crystals are common (Fig. 2D–E). Well-separated hexagonal platelets of a variety of crystalline states could also be observed in their intermediate phases (Fig. 2F–I). The slightly eroded edges of those thin hexagonal platelets on stalks (arrowed in Fig. 2F) showed an early stage of dissolution of GR crystals. Those euohedral hexagonal flakes were observed on a variety of structures, such as ferrihydrite spherules/rusticles (Fig. 2G) and stalks (Fig. 2C, F, and H). The TEM characterizations of crystal habits and SAED structures confirmed that the hexagonal crystals were GR. Abundant iron oxide aggregates on the relics of stalks (Fig. 3A, arrow a) and hexagonal flake crystals (Fig. 3A, arrow b) were also observed. The grey gradient in the TEM images shows the variation of thickness of the platelets (Fig. 3A–B). The inset hexagon of Fig. 3C yielded an ar-

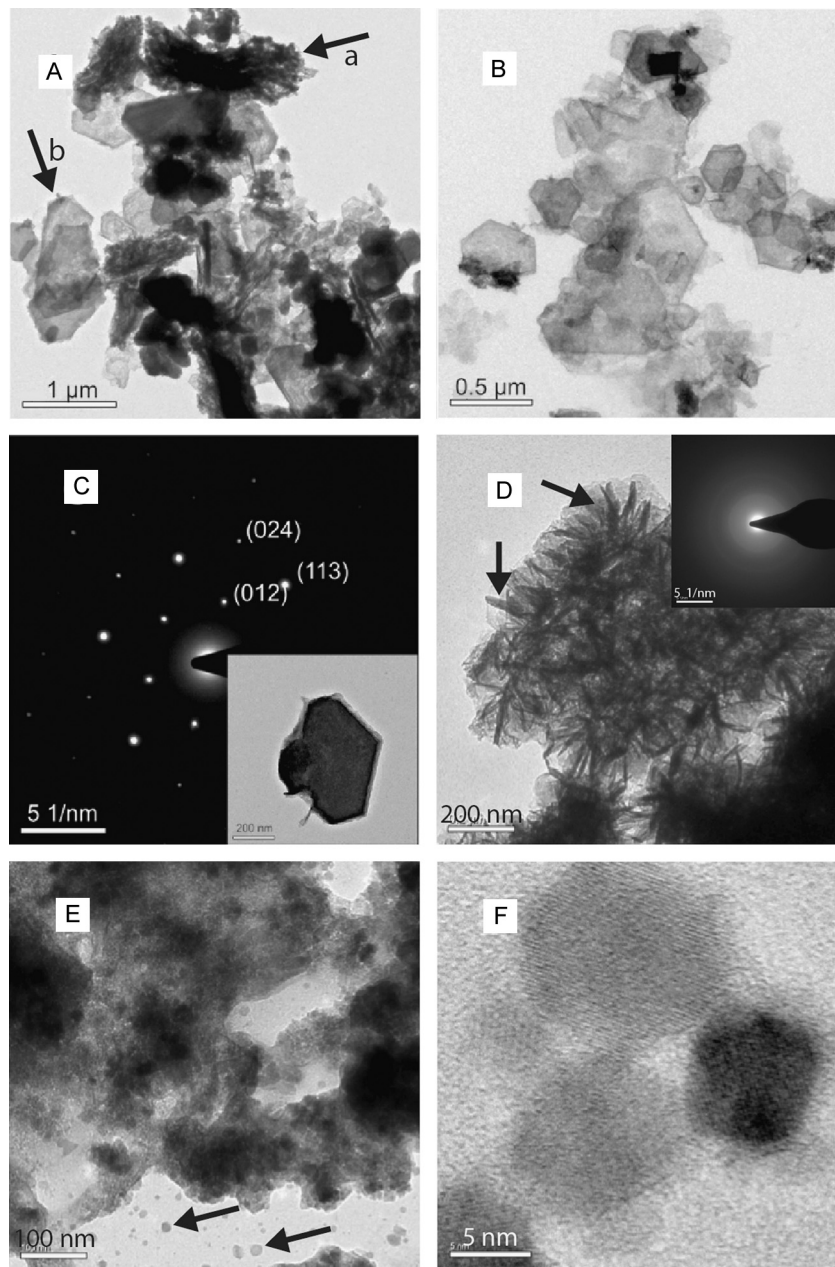


Fig. 3. TEM characterization of intermediate phases in the system of Fe(II)-oxidizing biomats reacted with Fe(II) under anaerobic condition. A. Relics of stalks (arrow a) together with GR flakes (arrow b) and fibrous organic materials covered by minerals (arrow c); B. The dissolving GR crystals; C. SAED pattern of one GR crystal, insert: the GR crystal for SAED measurement; D. Spikes and the early stage of GR crystallization. E. The formation the seed crystals of magnetite (arrowed) after the dissolution of GR. F. Magnetite nanocrystals at their early stage.

ray of SAED spots showing a monocrystal (Fig. 3C) with a set of Miller indices (hkl) of (024), (012) and (113) that match those of GR (e.g., Trolard et al., 2007). Immediately prior to the formation of GR, spikes (Fig. 3D) developed that were characterized by their amorphous nature as indicated by the diffuse rings in the SAED pattern (Fig. 3D inset). Along with the dissolution of GR, crystal seeds of magnetite emerged (Fig. 3E, arrowed), which then grew to ultrafine crystals of magnetite in a few hours (Fig. 3F).

A series of SEM observations captured the dissolution of GR and the subsequent crystallization of magnetite (Fig. 4). After the dissolution of GR, the sharp flaky and hexagonal structures were eroded to wafer surfaces (arrows in Fig. 4A–C, arrow a in Fig. 4D). With continuous decay, the GR platelets eventually dissolved completely (Fig. 4B–C). New isometric spheroidal aggregates containing magnetite nanocrystals (invisible under those amplifications) between

50 and 300 nm in size began to appear (arrow b in Fig. 4D and Fig. 4E–F). The collapse of these spherules upon further incubation showed the structures to be hollow (Fig. 4F), a feature completely different from the spherule/rusticles of ferrihydrite, but similar to the structure made of magnetite nanoparticles in previous mineral synthetic experiments (Guan et al., 2009). TEM characterization similarly demonstrate the transformation process (Fig. 5). Fig. 5A shows the development of the hexagonal crystals of GR from the platy aggregate containing randomly oriented spikes (arrowed); Fig. 5B shows the dissolution of the GR crystals; Fig. 5C shows the formation of magnetite aggregates appear as dense area under TEM; and Fig. 5D shows a SAED pattern of aggregative magnetite nanoparticles. Fig. 5E–F show the appearance of extremely fine magnetite seed crystals that grew within a few hours to crystals as large as 15 nm.

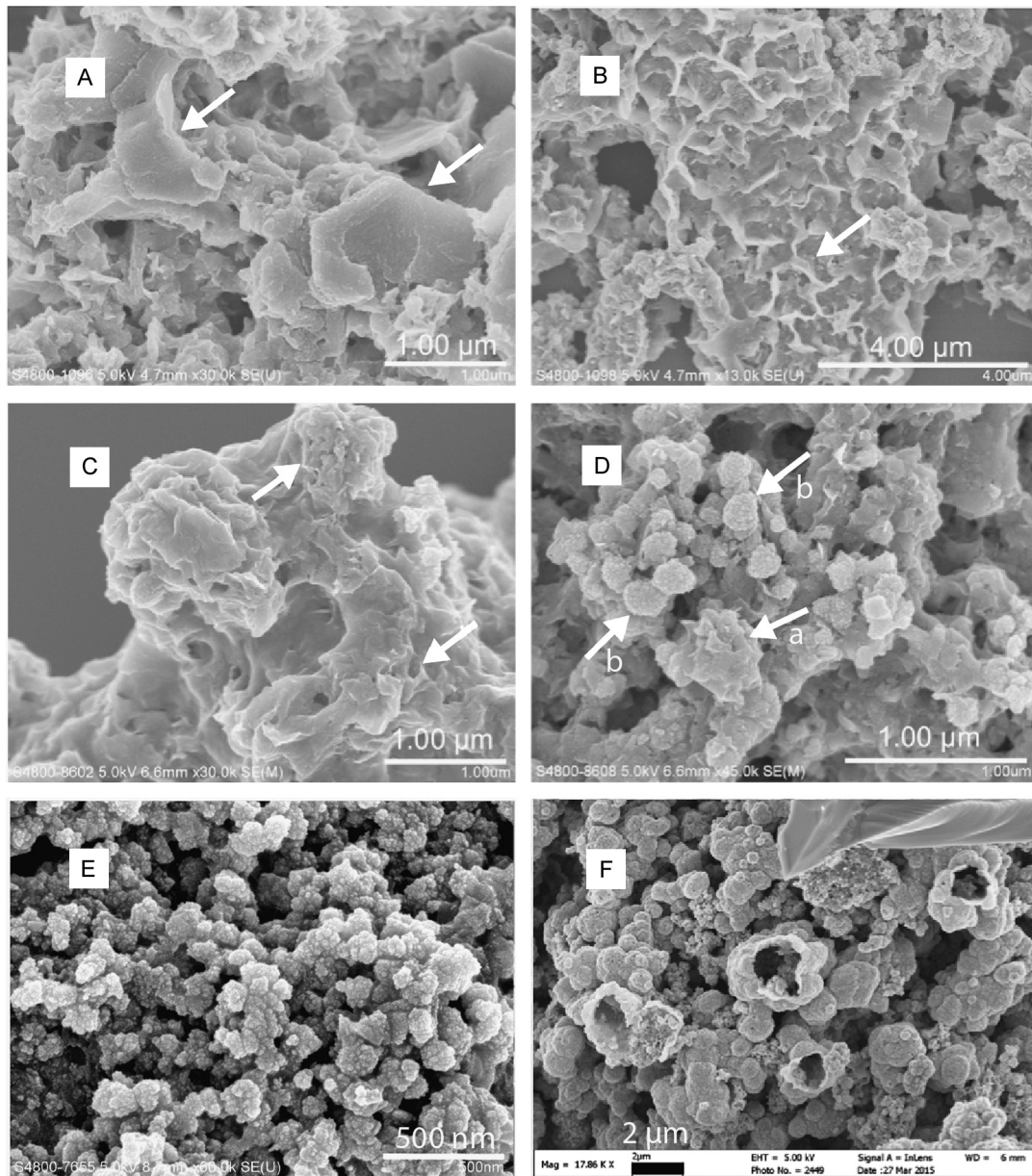


Fig. 4. SEM observations of the dissolving GR crystals and the production of invisible magnetite nanoparticles. A. Dissolving green rust crystals (arrowed); B. Relics of extensively-dissolved GR aggregates; C. Microenvironment without spherulitic structure after the dissolution of GR; D. Roughly isometric aggregates emerged after the dissolution of GR crystals; E. Aggregates contain magnetite nanoparticles (invisible); F. Broken spherules made of magnetite nanoparticles.

3.2. The structural confirmations of magnetite

XRD analyses showed the crystalline phase has a lattice constant of 8.396 Å. Together with the SAED results shown in Fig. 5D, this confirms that the end-product is magnetite. Detrital quartz from the environmental samples could also be detected by XRD (not shown). Mössbauer spectroscopy was used to detect possible amorphous iron minerals that could not be identified by SEM of particle size or confirmed by XRD for structure. The Mössbauer spectra of the end products of the 60 °C-batch experiments that were incubated for 20 h (Fig. 6A), 30 h (Fig. 6B) and 44 h (Fig. 6C) were similarly made of two sets of sextets of typical magnetite, and a quadrupole doublet ($IS = 0.30$ mm/s; $QS = 0.74$ mm/s) that represents the remaining ferrihydrite. No signal of GR could be detected by Mössbauer spectroscopy because of its instability upon oxidation. The sextet spectra of magnetite in Fig. 6A–C were not well developed because we purposely measured for a time long enough to identify magnetite but short enough to avoid the oxida-

tion of possible Fe^{2+} -excess magnetite (e.g., Li et al., 2011) during the measurements.

3.3. Experiments on the synthesized ferrihydrite and hematite extracted from BIF

The experiment where wet, chemically synthesized ferrihydrite was reacted with $Fe(II)$ was compared to the ferrihydrite-containing mats to assess similarities or differences of the reaction processes and products; while hematite extracted from BIF that was reacted with $Fe(II)$ was applied to compare with models on the reaction between hematite in BIF and metamorphic fluids containing $Fe(II)$ (e.g., Ohmoto, 2003). The end products of ferrihydrite+ $Fe(II)$ was also magnetite. The coexistence of magnetite clusters (arrowed) and hexagonal GR crystals were observed (Fig. 7A). The seed crystals of magnetite, as identified by high resolution TEM observation (Fig. 7B), were nucleated from the matrix of the dissolving GR that still contained rich fi-

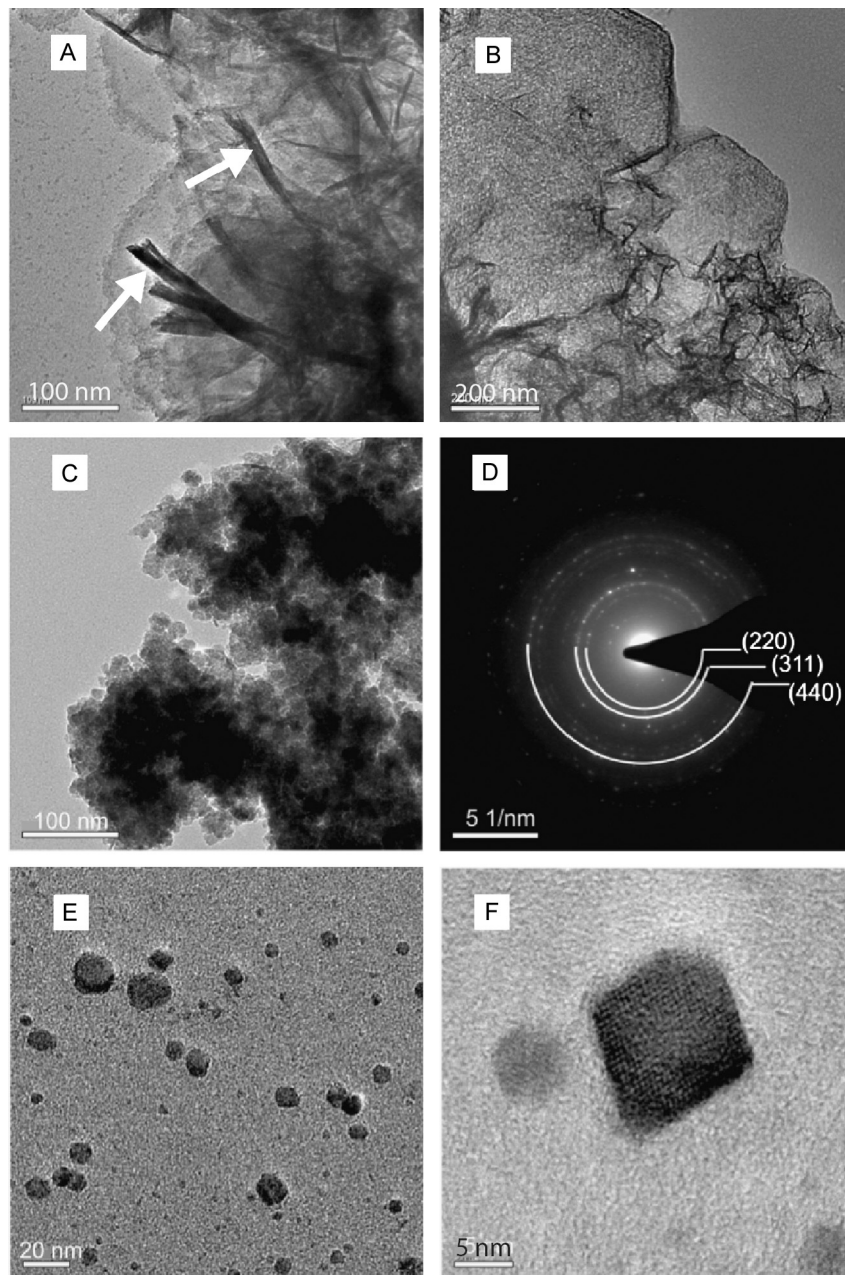


Fig. 5. TEM characterizations of magnetite the dissolution of GR. A. The remain of fibrous structure from the mat, GR crystals and the emergence of ultrafine crystal seeds of magnetite at left. B. Spikes (arrowed) and the early stage of GR dissolution. C. Aggregates containing magnetite which are too small to be shown; D. SAED pattern of the square in (A) showing magnetite was the only crystallized phase; E. Magnetite crystallized after the dissolving of GR crystals; F. Single crystal of magnetite.

brous spikes (Fig. 7C, the 'hairy' background). The high resolution TEM image showed clear lattice fringes that were indicative of their crystallinity (Fig. 7D). With further incubation, especially at high temperatures (50–60 °C), the magnetite crystal grew to >20 nm in diameter (Fig. 7E). The SAED pattern of one particle of >200 nm showed features of a monocrystal of magnetite (inset of Fig. 7F).

The long-term incubation of hematite + Fe(II) did not produce magnetite at the end of the one-month incubation. TEM imaging of the end product showed amorphous materials, including the dark diffusing plumes of Fe(II)-solution (Fig. 8A). The SAED pattern showed diffusive rings of amorphous nature (Fig. 8B). The hematite crystals still retained their lattice fringes (Fig. 8C) that yielded powder diffraction pattern of hematite nanoparticles (Fig. 8D).

3.4. The end product of ferrihydrite mats+Fe(II) systems

The reaction of ferrihydrite mats with Fe(II) under various conditions consistently produced magnetite of single domain size as the end product (Fig. 9A); this was confirmed by the SAED pattern (Fig. 9B). The small needle-like crystals were goethite (arrowed in Fig. 9A). The control experiment with ferrihydrite+Fe(II) also produced magnetite as the end product. As the control experiment, the ferrihydrite slurry without adding Fe(II) did not change its color, and neither did its mineralogical phase by the end of experimental time.

As control experiments, a few tubes were injected with 0.05 or 0.1 ml of air and shaken before the injection of Fe(II) stock solution. The injection of Fe(II) to those tubes also displayed a brief change in color to green and turned back to brown upon shaking. The SEM observations described in the following paragraph were

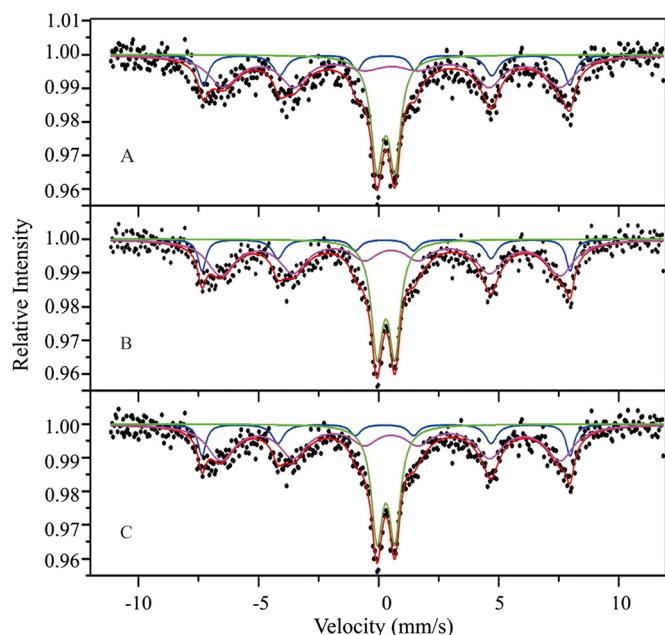


Fig. 6. The Mössbauer spectra of reaction products of *Gallionella* biomats reacted with Fe(II) under anaerobic condition after 20 h (A), 30 h (B) and 44 h (C). The sextets are of Fe^{3+} and $\text{Fe}^{2.5+}$ on magnetite and doublets are of Fe^{3+} on ferrihydrite.

also done on those samples, but the typical hexagonal crystals of green rust (GR) could not be observed in the subsamples sampled during incubations.

4. Discussions

4.1. Transformation from ferrihydrite to magnetite via green rust in the strict anaerobic media

Various iron oxides have been shown to react with dissolved Fe(II) under oxygen-free conditions to produce GR (e.g., Usman et al., 2012; Guilbaud et al., 2013), while the further transformation of GR into magnetite depends on the ratio of $\text{Fe(II)}/\sum\text{Fe}$ of GR (Guilbaud et al., 2013). For instance, after incubation at 70 °C for 7 days, GR with high $\text{Fe}^{2+}/\sum\text{Fe}$ (2/3) did not turn to magnetite (Géhin et al., 2002). GR has been widely reported to be the immediate product of microbial reduction of FeOOH species or ferrihydrite (Zegeye et al., 2012). In this study, the ferrihydrite mats that were reacted with Fe(II) under strictly anoxic conditions showed a clear intermediate phase of GR before the formation of magnetite (Figs. 2–3 and Fig. 5B). All experiments under either microoxic or fully oxic conditions failed to produce GR (as examined by SEM), and hence, no magnetite as the end-product, though the crystallinity of the original Fe(III)-oxides could be enhanced (Pedersen et al., 2005). These results clearly indicate that oxygen prohibits GR formation (Usman et al., 2012), and by extension, the prevention of magnetite mineralization by this pathway. According to Guan et al. (2009), spheroids such as those shown in Fig. 4D–E that form from GR dissolution transform into hollow spheres (Fig. 4F) containing magnetite nanoparticles. The measured XRD lattice constant was close to the perfect stoichiometry of magnetite [$\text{Fe}^{3+}(\text{Fe}^{3+}\text{Fe}^{2+})\text{O}_4$] by having a lattice constant = 8.396 Å. They are also very close to the perfect stoichiometric magnetite from the Dales Gorge Member BIF (Li et al., 2011).

GR generated from the ferrihydrite mats and chemically synthesized ferrihydrite reacting with dissolved Fe(II) all show further recrystallization to magnetite at temperatures 50–60 °C, indicating an insignificant role of organic matter in the ferrihydrite mats. The

order of the magnetite mineralization rates is ferrihydrite > ferric iron mats hematite. The slow reaction rate between ferrihydrite mats and Fe(II) could be the result of the retarding effect of some unknown organic compounds in the biomats (Jones et al., 2009). Similar to our results, Usman et al. (2012) did not detect magnetite by Mössbauer spectroscopy in the GR-containing media from reaction between hematite and water-soluble Fe(II). The lack of reaction between hematite and Fe(II) in this and previous studies (Pedersen et al., 2005) does not diminish the geochemical reaction between hematite and metamorphic Fe(II)-fluid during post-depositional processes (Ohmoto, 2003). However, according to the modal calculation by Morris (1985), using Fe(II)-containing fluids to magnetize massive hematite in BIF deposits requires unreasonably huge volumes of metamorphic fluids. Even when a potentially high influx of secondary fluids was included, petrologic observations showed that the $\text{Fe}^{3+}/(\text{Fe}^{3+} + \text{Fe}^{2+})$ of Fe-containing oxides and silicates assemblages did not change substantially when compared to BIFs that experienced low diagenetic to greenschist facies metamorphisms (Beukes et al., 2008). These findings are corroborated by the preservation of high heterogeneity of Fe-isotopic compositions in the micro-banding of BIFs (Frost et al., 2007).

4.2. Siliceous material in the products

Natural ferric oxyhydroxides often contain significant amounts of silica, and this was likely more so in the early Precambrian oceans due to extensive reactions between the hot seawater and the ultramafic marine crust (Konhauser et al., 2007; Rasmussen et al., 2015). In the intermediate phase of the ferrihydrite mats + Fe(II) experiments, some spiky structures and triangular-plane crystal phases were observed associated with the GR platelets. These were characterized by SEM and TEM as possibly Fe-rich siliceous materials (Fig. 2C). Similar structures have previously been described as “chlorite- or serpentine-like minerals”, or “Fe-rich, 7 Å-phyllsilicates” (De Jodin-Caumon et al., 2012). The crystal in Fig. 2C has composition and structure close to the mineral cronstedtite, and it is plausible that something mineralogically similar could have been a precursor phase to the iron silicates comprising some BIFs (e.g., Rasmussen et al., 2015).

4.3. Mineralization of magnetite in the ferruginous seawater column

There are petrologic, mineralogical and chemical lines of evidence that show magnetite in BIF is largely a secondary mineral (e.g. Morris, 1993; Johnson et al., 2008; Li et al., 2013; Li, 2014). Magnetite is generally presumed to have formed either as a result of biologically induced mineralization via DIR during early diagenesis (e.g., Konhauser et al., 2005; Johnson et al., 2008; Li et al., 2011) or through the abiogenic reduction of the precursor ferric oxyhydroxide phases with organic matter at temperatures exceeding the thresholds of DIR (e.g., Halama et al., 2016). Johnson et al. (2008) suggested that DIR probably emerged after ~2.9 Ga based on Fe-isotopes of magnetite in BIF, which was much later than the first appearance of the earliest BIF, e.g. 3.8-Ga Isua Supracrustal belt, Greenland (Frei and Polat, 2007; Czaja et al., 2013). At even higher temperatures, the decomposition of siderite to magnetite can take place, with or without the presence of organic carbon, while the transformation of hematite to magnetite requires a relatively high temperature (over 200 °C) along with the addition of Fe(II) derived from secondary hydrothermal or metamorphic fluids (Ohmoto, 2003; Klein, 2005; Frei and Polat, 2007). Within the timeframe of this experimental study, the reaction between hematite and dissolved Fe(II) was insignificant, which is consistent with the adsorption experiments and ^{55}Fe isotope traced reaction between hematite and aqueous Fe(II) (Pedersen et al., 2005).

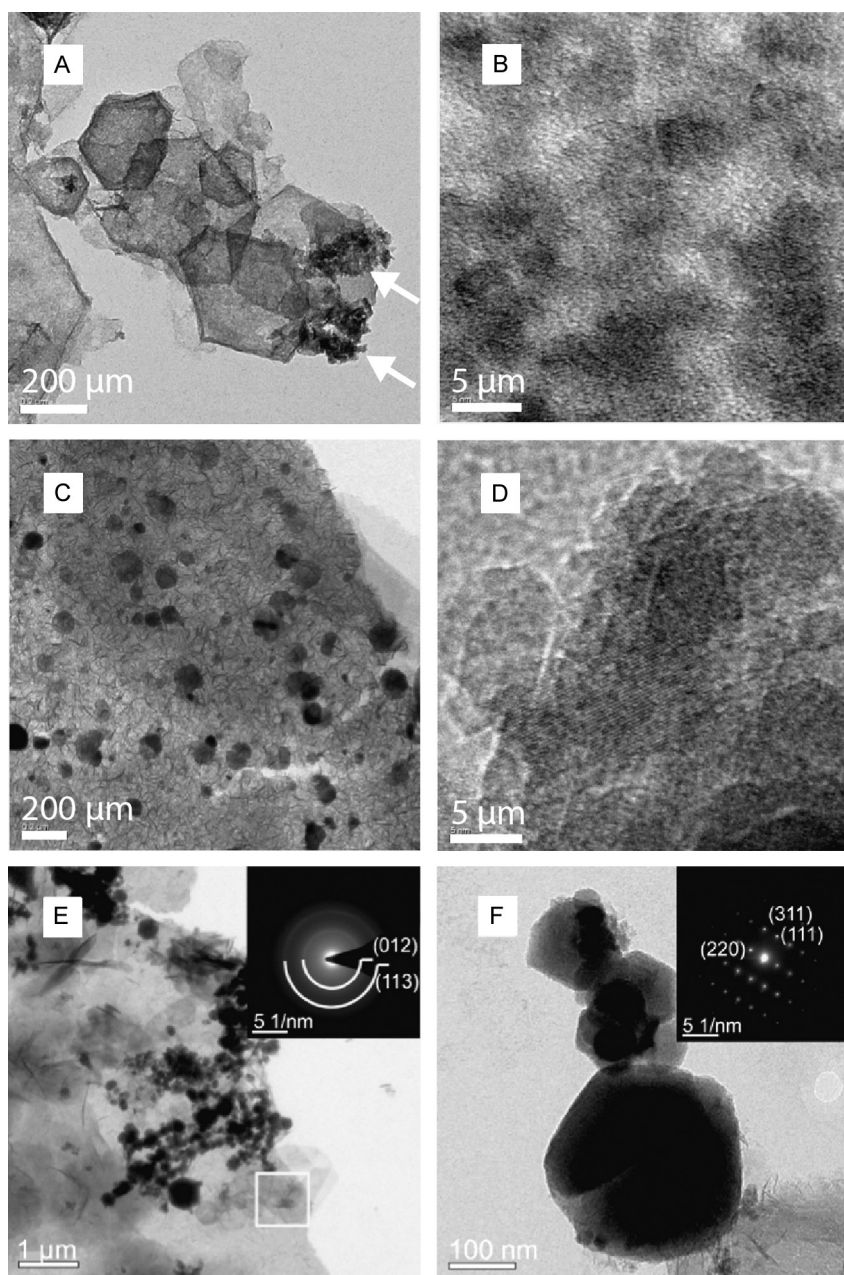


Fig. 7. TEM characterization of the evolution of mineral phases from GR to magnetite in experiments of synthetic ferrihydrite reacted with Fe(II) under strictly anaerobic condition. (A) The formation of GR. (B) The emergence of ultrafine magnetite crystals after the dissolution of GR. (C) Magnetite on the spike rich matrix. (D) High resolution observations showed lattice fringe of magnetite. (E) The formation of magnetite cluster, GR crystal on the background. Insert: SAED pattern of GR in squared area; (F) Magnetite crystals in the products, insert: SAED confirmed the structure of magnetite.

Based on this experimental study, we propose a new genetic model for some of the magnetite in BIF deposited in Archean (Fig. 10). We envision a marine photic zone where photoferrotrophs were the dominant marine plankton (Kappler et al., 2005); cyanobacteria, if existed, may have been present in “oxygen oases” as early as 3.0–3.2 Ga (Planavsky et al., 2014), but given the recent experimental findings indicates the high concentration of dissolved Fe(II) in the oceans may have been toxic to the cyanobacteria (Swanner et al., 2015). Through the photoferrotrophic oxidation of Fe(II), ferrihydrite was formed within the water column and then rapidly deposited onto the seafloor (Konhauser et al., 2005). During settling, some of the ferrihydrite was transformed into GR, which, in turn, converted to magnetite (Fig. 10). Importantly, only under reducing conditions could GR transform into magnetite because when GR reacts with oxygen it produces either ferrihydrite

or FeOOH species, such as goethite (Gémin et al., 1998). Thus, in areas where cyanobacteria may have been abundant (for instance the shallow shelf, either in the water column or as part of a stromatolite), it is unlikely that magnetite could have formed in the water column. This model is supported by the observation of a modern ferruginous water column of Lake Matano, Indonesia, in which photoferrotrophically produced ferrihydrite reacts with dissolved Fe(II) to produce GR, which in turn, transforms into magnetite within the water column (Zegeye et al., 2012). However, it is more likely that it was the episodic upwelling of the deep-sea hydrothermal waters enriched in dissolved Fe(II) that reacted with settling ferrihydrite particles, or those already deposited onto beneath the photic zone, that allowed magnetite to form prior to burial and diagenesis. The area and thickness of magnetite depended on the scale of the upwelling plume and the time it lasts. It is possible

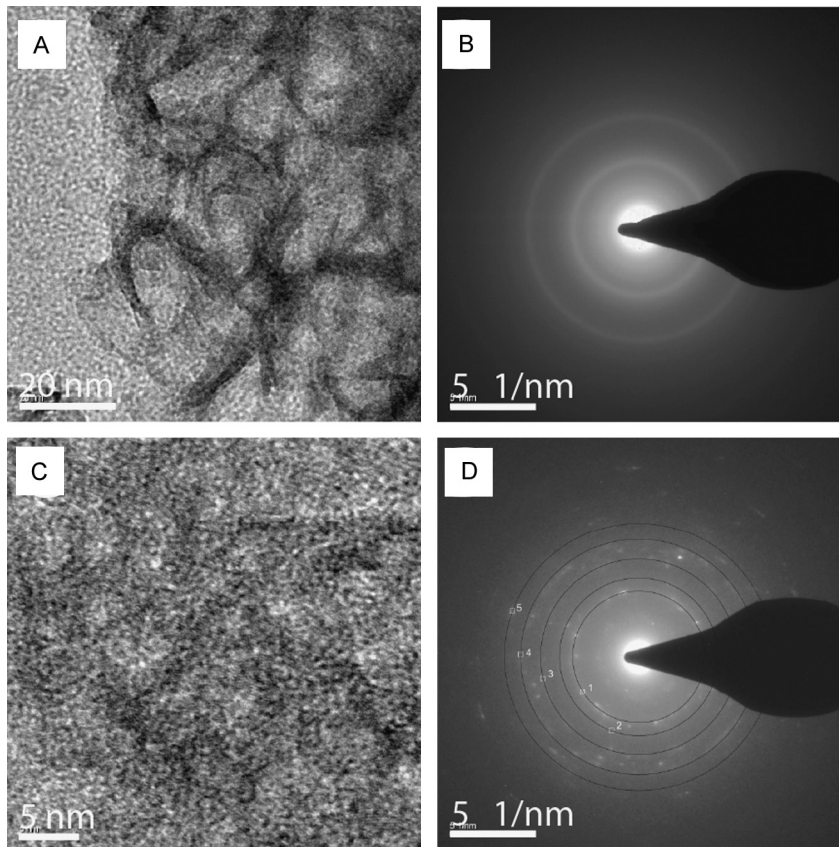


Fig. 8. TEM characterizations of the products of hematite interacting with Fe(II) under strict anaerobic condition. (A) Fibrous spikes on the interface between solid and the aqueous phase, no crystal of GR observed; (B) SAED showing amorphous material; (C) High resolution TEM observation showing lattice fringes of fine crystals of hematite. (D) SAED set of (hkl) consistent with hematite.

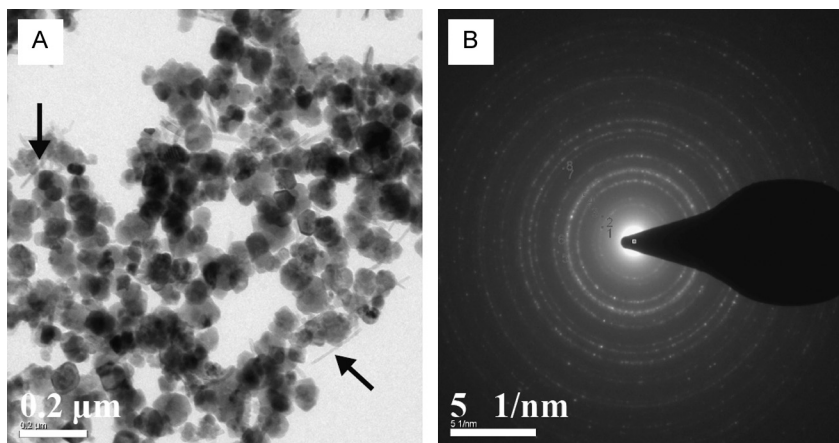


Fig. 9. The mineralization of single domain magnetite in experimental systems with $\text{pH} = 8.5$ and incubated at 60°C (A), confirmed by SAED (B). The arrowed nano-needles are goethite crystals.

that the concentration of Fe(II) dissolved in the ferruginous oceans was high enough to catalyze the recrystallization of ferrihydrite to a stable phase such as hematite (Pedersen et al., 2005) and therefore hematite bands in Archean BIFs (e.g., Sun et al., 2015), but not high enough to precipitate magnetite as we demonstrated in this study and elsewhere.

There are possible examples of this mechanism in the Archean rock record, including ~ 3.7 Ga BIFs from the Isua Supracrustal Belt in Western Greenland (Frei and Polat, 2007; Czaja et al., 2013), 3.05–2.95 Ga Mount Gibson BIF in Western Australia (Lascelles, 2006), and the 2.98 Ga West Rand Group of the Witwatersrand Supergroup, South Africa (Smith et al., 2013). For our mechanism

to be valid, hot, Fe(II)-enriched seawater was required, but importantly, the entire ocean water column did not have to be similar. Rather, various geochemical observations indicate that the iron in Archean BIFs was initially sourced from submarine hydrothermal fluids which not only provided Fe(II) but also the (episodic) high temperature plumes that might facilitate the magnetization of GR. Supporting this scenario are various geochemical features in BIFs, including, REE pattern, $\epsilon\text{Nd}(t)$ and Ge/Si ratios (Danielson et al., 1992; Hamade et al., 2003; Frei and Polat, 2007).

This genetic model of magnetite in the Archean BIF also explains the debated origin to the banding characteristic of BIFs, i.e., the micro- to mesobands of both magnetite (Morris, 1993;

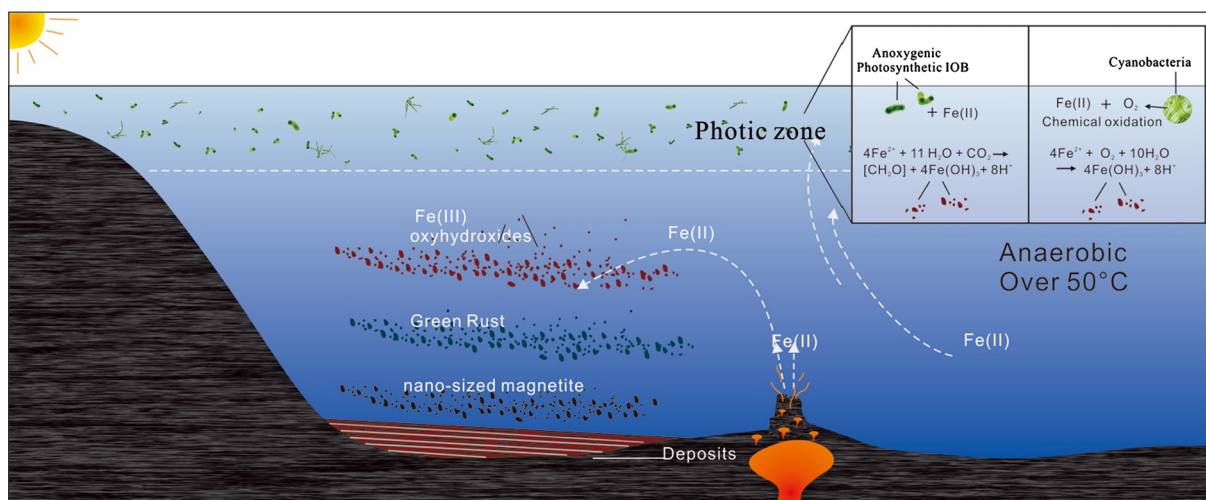


Fig. 10. Schematic showing magnetite from ferruginous Archean photoferrotothy or oxygenic photosynthesis.

Smith et al., 2013; Li, 2014) and hematite (Ewers and Morris, 1981; Gole, 1981; Pecoits et al., 2009; Li, 2014). We suggest that in some cases the magnetite were made in the ocean's water column through the reaction of photoferrotothy-generated with hot, Fe(II)-high fluids sourced from hydrothermal vents. In this regard, more vigorous mantle recycling and volcanic eruptions on the early Earth (Isley and Abbott, 1999) would not only have impacted the composition of the oceans, but also the supply of hydrothermal sourced Fe(II) to the bulk oceans. In the case of the former, it has been suggested that the early Archean was characterized by a hotter mantle which led to a thicker ocean lithosphere, perhaps 20 km thick (Sleep and Windley, 1982). If the elevation of mid ocean ridges (MORs) increases 1 km for every additional 6–10 km lithospheric thickness (Sleep and Windley, 1982), then Archean MORs had elevations much shallower than today. With MOR crust perhaps only 500 m deep, hydrothermal plumes could have been introduced directly to the upper oceans at depths generally consistent with the depth of BIF deposition (Isley and Abbott, 1999). So the Fe(II)-richer ocean indicated by Fe-isotopic composition in magnetite of the Isua BIF (Czaja et al., 2013) might be a reflection of input of seafloor vented Fe(II)-high fluids with high frequency and large scale. As radiogenic heat in the interior Earth decreased, MOR depth increased, such that ridge crusts withdrew from the upper ocean. As the introduction of hydrothermally introduced Fe to upper ocean waters ended, it diminished the likelihood of Fe(II) being effused directly to the shallow oceans. Thereafter, as ferrihydrite formed in the water column, it would have settled to the seafloor without having come into contact with Fe(II)-high plumes from hydrothermal vent. Ferrihydrite would then have been dehydrated to bands of hematite or settled along with cell biomass, leading to secondary magnetite formation via DIR. As an example, the iron-rich bands of the Dales Gorge BIF is predominantly made of hematite, while the magnetite micro- or macrobands appear episodically (Pecoits et al., 2009; Li, 2014).

5. Conclusions

We report the interactions between ferric iron oxide mats and soluble Fe(II) under strictly anaerobic condition as an analogue to the interaction between the photoferrotothy oxidized Fe(III) and Fe(II)-rich, hot fluids from the hydrothermal vents in Archean. Our experimental results demonstrate that the reactions lead to the formation of magnetite via an intermediate green rust phase. This pathway could explain why early Archean Precambrian BIFs contain abundant magnetite due to the higher frequency and amount

of discharged hot, Fe(II)-rich waters into the oceans. By contrast, the deposition of hematite bands reflects a lack of interaction between Fe(II) and ferric oxyhydroxide precipitated from photosynthetic Fe(II)-oxidation. As magnetite carries 2/3 Fe as Fe³⁺ inherited from photoferrotothy precipitated iron oxide, magnetite of the Isua BIF can be considered the oldest lithological signature of life on Earth.

Acknowledgements

We thank Bertus Smith of the University of Johannesburg, Bruce Simonson of Oberlin College and an anonymous reviewer for their very insightful comments that greatly improved our manuscript. We thank Dr. J. Li for her assistance with experiments and part of electron microscopic observations. YLL was supported by General Research Fund (HKU702913P) from Research Grants Council of Hong Kong, KOK was supported by a Discovery Grant from the Natural Sciences and Engineering Research Council of Canada (DG165831), and MGZ was supported by the Chinese Academy of Sciences (XDB18030205 & QYZDY-SSW-DQco17).

References

- Bekker, A., Planavsky, N.J., Krapež, B., Rasmussen, B., Hofmann, A., Slack, J.F., Rouxel, O.J., Konhauser, K.O., 2014. Iron formation: their origins and implications for ancient seawater chemistry. In: Holland, H.D., Turkian, K.K. (Eds.), *Treatise in Geochemistry*, 2nd edition, vol. 9. Elsevier, Amsterdam, pp. 561–628.
- Bekker, A., Slack, J.F., Planavsky, N., Krapež, B., Hofmann, A., Konhauser, K.O., Rouxel, O.J., 2010. Iron formation: the sedimentary product of a complex interplay among mantle, tectonic, oceanic, and biospheric processes. *Econ. Geol.* 105, 467–508.
- Beukes, N.J., Mukhopadhyay, J., Gutzmer, J., 2008. Genesis of high-grade iron ores of the Archean Iron Ore Group around Noamundi, India. *Econ. Geol.* 103, 365–386.
- Butler, I.B., Schoonen, M.A.A., Richard, D.T., 1994. Removal of dissolved oxygen from water: a comparison of four common techniques. *Talanta* 41, 211–215.
- Czaja, A.D., Johnson, C.M., Beard, B.L., Roden, E.E., Li, W., Moorbath, S., 2013. Biological Fe oxidation controlled deposition of banded iron formation in the ca. 3770 Ma Isua Supracrustal Belt (West Greenland). *Earth Planet. Sci. Lett.* 363, 192–203.
- Danielson, A., Möller, P., Dulski, P., 1992. The europium anomalies in banded iron formations and the thermal history of the oceanic crust. *Chem. Geol.* 97, 89–100.
- De Jodin-Caumon, M.-C., Mosser-Ruck, R., Randi, A., Pierron, O., Cathelineau, M., Michau, N., 2012. Mineralogical evolution of a claystone after reaction with iron under thermal gradient. *Clays Clay Miner.* 60, 443–455.
- Derry, L.A., Jacobsen, S.B., 1990. The chemical evolution of Precambrian seawater: evidence from REEs in banded iron formations. *Geochim. Cosmochim. Acta* 54, 2965–2977.
- Ewers, W.E., Morris, R.C., 1981. Studies of the Dales Gorge member of the Brockman iron formation, Western Australia. *Econ. Geol.* 76, 1929–1953.
- Frei, R., Polat, A., 2007. Source heterogeneity for the major components of ~3.7 Ga banded iron formations (Isua Greenstone Belt, Western Greenland): tracing the

- nature of interacting water masses in BIF formation. *Earth Planet. Sci. Lett.* 253, 266–281.
- Frost, C.D., von Blanckenburg, F., Schoenberg, R., Frost, B.R., Swapp, S.M., 2007. Preservation of Fe isotope heterogeneities during diagenesis and metamorphism of banded iron formation. *Contrib. Mineral. Petrol.* 153, 211–235.
- Géhin, A., Ruby, C., Abdelmoula, M., Benali, O., Ghanbaja, J., Refait, P., Génin, J.-M.R., 2002. Synthesis of Fe(II–III) hydroxysulphate green rust by coprecipitation. *Solid State Sci.* 4, 61–66.
- Génin, J.-M.R., Bourrié, G., Trolard, F., Abdelmoula, M., Jaffrezic, A., Refait, P., Herbillon, A., 1998. Thermodynamic equilibria in aqueous suspensions of synthetic and natural Fe(II)–Fe(III) green rusts: occurrences of the mineral in hydromorphic soils. *Environ. Sci. Technol.* 32, 1058–1068.
- Gole, M.J., 1981. Archean banded iron-formations, Yilgarn Block, Western Australia. *Econ. Geol.* 76, 1954–1974.
- Gross, G.A., 1986. The metallogenetic significance of iron-formation and related stratafer rocks. *J. Geol. Soc. India* 28, 92–108.
- Guan, N., Wang, Y., Sun, D., Xu, J., 2009. A simple one-pot synthesis of single-crystalline magnetite hollow spheres from a single iron precursor. *Nanotechnology* 20, 105603, 8 pp.
- Guilbaud, R., White, M.L., Poulton, S.M., 2013. Surface charge and growth of sulphate and carbonate green rust in aqueous media. *Geochim. Cosmochim. Acta* 108, 141–153.
- Halama, M., Swanner, E.D., Konhauser, K.O., Kappler, A., 2016. Evaluation of siderite and magnetite formation in BIFs by pressure–temperature experiments of Fe(III) minerals and microbial biomass. *Earth Planet. Sci. Lett.* 450, 243–253.
- Hamade, T., Konhauser, K.O., Raiswell, R., Goldsmith, S., Morris, R.C., 2003. Using Ge/Si ratios to decouple iron and silica fluxes in Precambrian banded iron formations. *Geology* 31, 35–38.
- Isley, A.E., Abbott, D.H., 1999. Plume-related mafic volcanism and the deposition of banded iron formation. *J. Geophys. Res.* 104, 15461–15477.
- Jacobsen, S.B., Pimentel-Klose, M.R., 1988. A Nd isotopic study of the Hamersley and Michipicoten banded iron formations: the source of REE and Fe in Archean oceans. *Earth Planet. Sci. Lett.* 87, 29–44.
- Johnson, C.M., Beard, B.L., Roden, E.E., 2008. The iron isotope fingerprints of redox and biogeochemical cycling in modern and ancient Earth. *Annu. Rev. Earth Planet. Sci.* 36, 457–493.
- Jones, A.M., Collins, R.N., Rose, J., Waite, T.D., 2009. The effect of silica and natural organic matter on the Fe(II)-catalysed transformation and reactivity of Fe(III) minerals. *Geochim. Cosmochim. Acta* 73, 4409–4422.
- Kappler, A., Pasquero, C., Konhauser, K.O., Newman, D.K., 2005. Deposition of banded iron formations by anoxygenic phototrophic Fe(II)-oxidizing bacteria. *Geology* 33, 865–868.
- Klein, C., 2005. Some Precambrian banded iron-formations (BIFs) from around the world: their age, geologic setting, mineralogy, metamorphism, geochemistry, and origins. *Am. Mineral.* 90, 1473–1499.
- Knauth, L.P., 2005. Temperature and salinity history of the Precambrian ocean: implications for the course of microbial evolution. *Palaeogeogr. Palaeoclimatol. Palaeoecol.* 219, 53–69.
- Konhauser, K.O., Amskold, L., Lalonde, S.V., Posth, N.R., Kappler, A., Anbar, A., 2007. Decoupling photochemical Fe(II) oxidation from shallow-water BIF deposition. *Earth Planet. Sci. Lett.* 258, 87–100.
- Konhauser, K.O., Newman, D., Kappler, A., 2005. The potential significance of microbial Fe(III) reduction during deposition of Precambrian banded iron formations. *Geobiology* 3, 167–177.
- Krapež, H., Barley, M.E., Pickard, A.L., 2003. Hydrothermal and resedimented origins of the precursor sediments to banded iron formation: sedimentological evidence from the early Palaeoproterozoic Brockman Supersequence of Western Australia. *Sedimentology* 50, 979–1011.
- Lascelles, D.F., 2006. The Mount Gibson banded iron formation-hosted magnetite deposit: two distinct processes for the origin of high-grade ore. *Econ. Geol.* 101, 651–666.
- Li, Y.L., 2014. Micro- and nanobands in late Archean and Palaeoproterozoic banded-iron formations as possible mineral records of annual and diurnal depositions. *Earth Planet. Sci. Lett.* 391, 160–170.
- Li, Y.-L., Konhauser, K.O., Cole, D.R., Phelps, T.J., 2011. Mineral ecophysiological data provide growing evidence for microbial activity in banded-iron formations. *Geology* 39, 707–710.
- Li, Y.-L., Konhauser, K.O., Kappler, A., Hao, X.-L., 2013. Experimental low-grade alteration of biogenic magnetite indicates microbial involvement in generation of banded iron formations. *Earth Planet. Sci. Lett.* 361, 229–237.
- Lv, K.P., Norman, L., Li, Y.L., 2016. Restrictions on the production of multi-wall carbon nanotubes and nanofibers by *Gallionella* sp. *Geomicrobiol. J.* 33, 709–715.
- Morris, R.C., 1985. Genesis of iron ore in banded iron-formation by supergene and supergene-metamorphic processes – a conceptual model. In: Meurant, G. (Ed.), *Handbook of Strata-Bound and Stratiform Ore Deposits. In: Regional Studies and Specific Deposits*, vol. 13, pp. 73–235.
- Morris, R.C., 1993. Genetic modelling for banded iron-formation of the Hamersley Group, Pilbara Craton, Western Australia. *Precambrian Res.* 60, 243–286.
- Ohmoto, H., 2003. Nonredox transformations of magnetite–hematite in hydrothermal systems. *Econ. Geol.* 98, 157–161.
- Pedersen, H.D., Postma, D., Jakobsen, R., Larsen, O., 2005. Fast transformation of iron oxyhydroxides by the catalytic action of aqueous Fe(II). *Geochim. Cosmochim. Acta* 69, 3967–3977.
- Pecoits, E., Gingra, M.K., Barley, M.E., Kappler, A., Posth, N.R., Konhauser, K.O., 2009. Petrography and geochemistry of the Dales Gorge banded iron formation: paragenetic sequence, source and implications for palaeo-ocean chemistry. *Precambrian Res.* 172, 163–187.
- Pecoits, E., Smith, M.L., Catling, D.C., Philippot, P., Kappler, A., Konhauser, K.O., 2015. Atmospheric hydrogen peroxide and Eoarchean iron formations. *Geobiology* 13, 1–14.
- Pignatelli, I., Mugnaioli, E., Hybler, J., Mosser-Ruck, R., Cathelineau, M., Michau, N., 2013. A multi-technique characterization of cronstedtite synthesized by iron-clay interaction in a step-by-step cooling procedure. *Clays Clay Miner.* 61, 277–289.
- Planavsky, N.J., Asael, D., Hofmann, A., Reinhard, C.T., Lalonde, S.V., Knudsen, A., Wang, X., Ossa Ossa, F., Pecoits, E., Smith, A.J.B., Beukes, N.J., Bekker, A., Johnson, T.M., Konhauser, K.O., 2014. Evidence for oxygenic photosynthesis half a billion years before the Great Oxidation Event. *Nat. Geosci.* 7, 283–286.
- Rasmussen, B., Krapež, B., Muhling, J.R., Suvorova, A., 2015. Precipitation of iron silicate nanoparticles in early Precambrian oceans marks Earth's first iron age. *Geology* 43, 303–306.
- Sleep, N.H., Windley, B.F., 1982. Archean plate tectonics: constrains and inferences. *J. Geol.* 90, 363–379.
- Smith, A.J.B., Beukes, N.J., Gutzmer, J., 2013. The composition and depositional environments of Mesoarchean Iron Formations of the West Rand Group of the Witwatersrand Supergroup, South Africa. *Econ. Geol.* 108, 111–134.
- Sun, S., Konhauser, K.O., Kappler, A., Li, Y.L., 2015. Primary hematite in Neoproterozoic oceans. *Geol. Soc. Am. Bull.* 127, 850–861.
- Swanner, E.D., Wu, W., Hao, L., Wustner, M.L., Obst, M., Moran, D.M., McIlvin, M.R., Saito, M.A., Kappler, A., 2015. Physiology, Fe(II) oxidation, and Fe mineral formation by a marine planktonic cyanobacterium grown under ferruginous conditions. *Front. Earth Sci.* 3, 60, 1–21.
- Trolard, F., Bourrié, G., Abdelmoula, M., Refait, P., Feder, F., 2007. Fougerite, a new mineral of the pyroaurite-iowaite group: description and crystal structure. *Clays Clay Miner.* 55, 323–334.
- Usman, M., Hanna, K., Abdelmoula, M., Zegeye, A., Faure, P., Ruby, C., 2012. Formation of green rust via mineralogical transformation of ferric oxides (ferrihydrite, goethite and hematite). *Appl. Clay Sci.* 64, 38–43.
- Zegeye, A., Bonneville, S., Benning, L.G., Strum, A., Fowle, D.A., Jones, C., Canfield, D.E., Ruby, C., MacLean, L.C., Nomosatroy, S., Crowe, S.A., Poulton, S.W., 2012. Green rust formation controls nutrient availability in a ferruginous water column. *Geology* 40, 599–602.